



www.sciencemag.org/cgi/content/full/331/6014/186/DC1

Supporting Online Material for

Observation of Half-Height Magnetization Steps in Sr_2RuO_4

J. Jang, D. G. Ferguson, V. Vakaryuk, R. Budakian,* S. B. Chung, P. M. Goldbart,
Y. Maeno⁴

*To whom correspondence should be addressed. E-mail: budakian@illinois.edu

Published 14 January 2010, *Science* **331**, 186 (2010)
DOI: 10.1126/science.1193839

This PDF file includes:

Materials and Methods

SOM Text

Figs. S1 to S10

Tables S1 and S2

References

Supporting Online Material for

Observation of half-height magnetization steps in Sr_2RuO_4

J. Jang, D.G. Ferguson, V. Vakaryuk, R. Budakian^{*}, S.B. Chung, P.M. Goldbart, and Y. Maeno

^{*} To whom correspondence should be addressed. E-mail: budakian@illinois.edu

This PDF file includes:

Materials and Methods

SOM Text

Figs. S1 to S10

Tables S1 and S2

References

Materials and Methods

The micron-sized annular Sr_2RuO_4 samples were obtained from millimeter-sized crystals grown using the floating-zone method (*SI*). The SRO crystal was first glued to a post, then $\sim 100\text{-}\mu\text{m}$ thick segments were cleaved using a razor blade. To avoid possible oxidation and surface contamination, only segments obtained from the interior of the larger crystal were used. The SRO segment was crushed on a silicon substrate and the pieces were imaged using the electron beam of a dual-column focused ion beam (FIB). The shape of the particles was found to be an important factor in determining the orientation of crystalline axis; for the particles used in this study, the orientation of the *ab* planes was clearly visible from the layering observed near the edges of the particle. Figure S1A is an example of a low magnification SEM image showing the particle distribution (after crushing), which was later used as a map to identify the location of the FIB-ed particle under optical microscope. Higher magnification SEM scans from various angles were necessary to confirm the layering of a particle. After locating the desired particle, the 30 kV ion source was used to cut a hole in the center of the particle parallel to the crystal *c*-axis. In order to minimize ion implantation, the number of images taken using the ion source was limited to two exposures at emission current of 1 pA; the hole was cut using an emission current of 10 pA. The milled particle was then transferred to a micro-manipulator stage of a long working distance Mitutoyo optical microscope. The FIB-ed particle was located from the pattern of the debris field

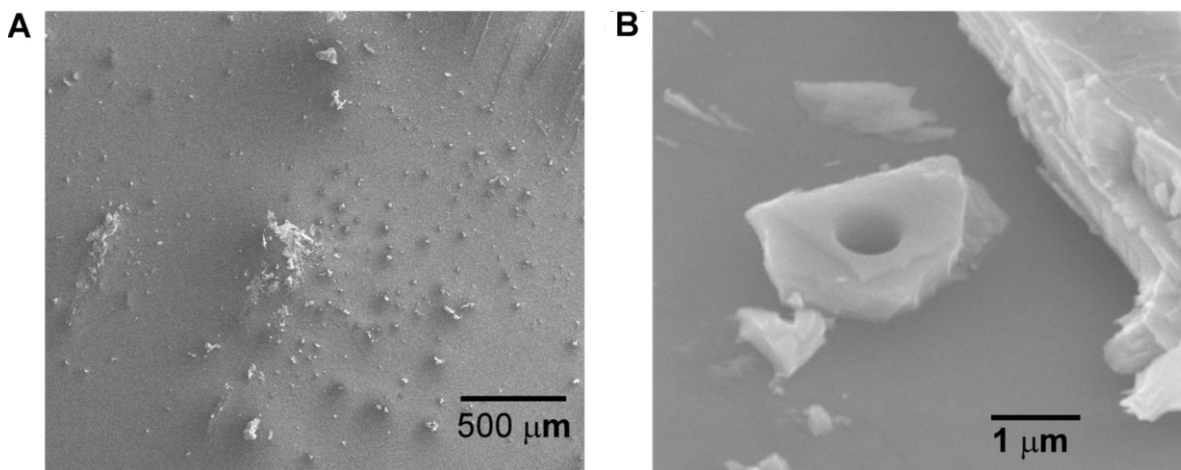
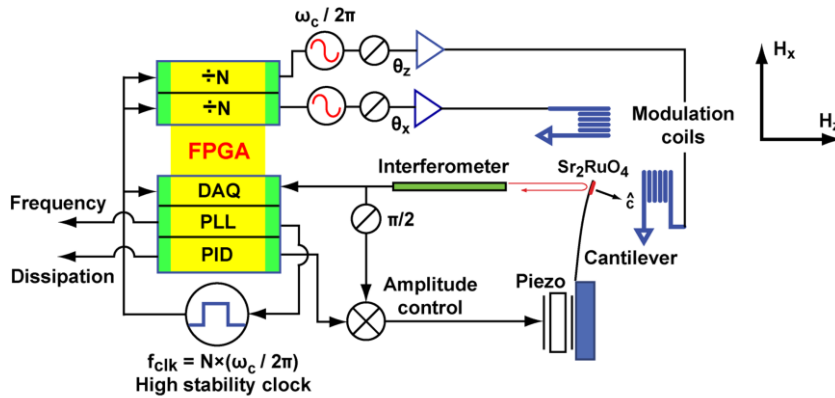


Figure S1: (A) Low magnification SEM of SRO debris field. (B) A micron-size SRO particle after cutting a hole using the FIB.

imaged using the SEM. A three-axis hydraulic Narishige micromanipulator was used to position a pulled borosilicate micropipette having a $< 1 \mu\text{m}$ tip diameter near the particle. The electrostatic interaction of the particle with the micropipette was sufficient to pick up the particle. The particle was glued to the tip of a custom-fabricated silicon cantilever. Prior to placement of the particle, a small amount of Gatan G-1 epoxy was placed on the tip of the cantilever. The epoxy was cured overnight at 70°C in a nitrogen environment. The planar geometry of the particle ensured that the particle's c -axis was oriented perpendicular to the axis of the cantilever. However, the a and b axes had no special orientation with respect to the cantilever.

Phase-locked cantilever magnetometry

In the presence of an external magnetic field \mathbf{H} , the cantilever is subject to a torque $\boldsymbol{\tau} = \boldsymbol{\mu} \times \mathbf{H}$ produced by the magnetic moment $\boldsymbol{\mu}(\mathbf{H})$ of the superconductor. During measurement, the cantilever is placed in a positive feedback loop, and is driven at its natural frequency using a piezoelectric transducer; the resulting tip motion is given by $z(t) = z_{pk} \cos \omega_c t$. To enhance detection sensitivity, a small time-dependent magnetic field $\delta H(t)$ is applied perpendicular to the component of $\boldsymbol{\mu}$ that we seek to detect. By making $\delta H(t)$ depend on the phase of the cantilever position, the cantilever experiences a dynamic position-dependent force, which shifts either the cantilever frequency or its dissipation. In general, the applied modulation can be of the form: $\delta \mathbf{H}(t) = \delta H_x \cos(\omega_c t + \theta_x) \hat{x} + \delta H_z \cos(\omega_c t + \theta_z) \hat{z}$, where the phase angles θ_x and θ_z can be independently chosen. We refer the reader to a more detailed treatment of phase-locked



cantilever magnetometry in ref. In the presence of a static magnetic field $\mathbf{H} = H_x \hat{x} + H_z \hat{z}$ and the applied modulation $\delta \mathbf{H}(t)$, the Fourier transform of the equation of motion of the cantilever is given by:

Figure S2: Schematic of phase-locked cantilever magnetometry apparatus.

$$\begin{aligned}
& (-m\omega^2 - im\gamma\omega + k)\tilde{z}(\omega) \\
&= \frac{1}{L_{eff}^2} \{(\mu_x - \chi_c H_x)H_x + (\mu_z - \chi_{ab} H_z)H_z\} \tilde{z}(\omega) \\
&+ \frac{1}{L_{eff} z_{pk}} \{(\mu_x - \chi_c H_x)\delta H_z e^{i\theta_z} + (\mu_z - \chi_{ab} H_z)\delta H_x e^{i\theta_x}\} \tilde{z}(\omega).
\end{aligned} \tag{S1}$$

Here, k , $m = k/\omega_c^2$, and $L_e (\approx L/1.38)$ are the cantilever spring constant, effective mass and effective length, respectively; μ_x and μ_z are the c -axis and ab -plane components of the magnetic moment and χ_c and χ_{ab} are the two components of the magnetic susceptibility of the sample. We note that for our samples $\chi_c \gg \chi_{ab}$. This assumption is justified because of the large shape anisotropy of our sample as well as the highly anisotropic response of the superconductor: $\gamma_{SC} = \lambda_c(0)/\lambda_{ab}(0) \approx 20$, where $\lambda_c(0) = 3.0 \times 10^3$ nm and $\lambda_{ab}(0) = 152$ nm are the zero temperature c -axis and ab -plane penetration depths, respectively (S1). In writing Eq. (S1), we have assumed that the peak angle of the cantilever deflection is $z_{pk}/L_{eff} \ll 1$. In our measurements, $L_{eff} \approx 55$ μm and $z_{pk} \approx 60$ nm, thus the assumption of small angles is justified. The static magnetic fields applied in the lab reference frame generate position-dependent fields in the oscillating reference frame of cantilever in addition to the applied modulation. To ensure that the magnetic field in the reference frame of the SRO sample has the desired time-dependence, both feedback and feed-forward modulation is applied in the x and z directions.

To measure the c -axis moment, we modulate the in-plane field by $\delta H_x = 1.0$ Oe; the relative phase is chosen so as to shift the cantilever dissipation γ : $\theta_x = \pi/2$. An expression for the shift in dissipation is obtained from Eq. (S1)

$$\Delta\gamma_z = \frac{\omega_c}{kL_{eff}z_{pk}} \delta H_x (\mu_z - \chi_{ab} H_z) \tag{S2}$$

In the regime that the superconductor exhibits linear response, $\mu_z = \Delta\mu_z n + \chi_c H_z$, where n is the fluxoid quantum number and $\Delta\mu_z$ is the change in the magnetic moment of the ring associated with fluxoid entry. Since $\chi_c \gg \chi_{ab}$, Eq. (S2) reduces to

$$\Delta\gamma_z \approx \frac{\omega_c}{kL_{eff}z_{pk}} \delta H_x (\Delta\mu_z n + \chi_c H_z). \quad (S3)$$

To measure the *ab*-plane moment, we modulate the *c*-axis field by $\delta H_z = 1.0$ Oe; the relative phase is also chosen to be $\theta_z = \pi/2$. The expression for the shift in dissipation is given by

$$\Delta\gamma_x \approx \frac{\omega_c}{kL_{eff}z_{pk}} (\mu_x - \chi_c H_x) \delta H_z. \quad (S4)$$

The phase-locked cantilever magnetometry technique can also be used to measure the derivative $d\mu/dH$; derivative measurements are particularly useful in studying non-hysteretic (i.e., reversible) magnetic variations; under certain conditions, derivative measurements can yield higher signal-to-noise ratio than the direct measurements of magnetic moment discussed above. In this work, we employ derivative measurements to study the high temperature behavior of the fluxoid transitions presented in Fig. 3C of the main text. For the derivative measurements, a small phase-locked modulation $\delta H_z(t)$ is applied parallel to the *c*-axis of the sample. In the presence of a non-zero static in-plane magnetic field H_x , the position-dependent magnetic moment produced by $\delta H_z(t)$ shifts the cantilever dissipation by

$$\Delta\gamma_x \approx \frac{\omega_c}{k L_{eff} z_{pk}} (\mu_x - \chi_c H_x) \delta H_z \quad (S5)$$

If we neglect the term $d\mu_x/dH_z$, and provided the modulation amplitude is sufficiently small, the above equation reduces to

$$\Delta\gamma_x \approx -\frac{\omega_c}{k L_{eff} z_{pk}} \left(\frac{d\mu_z}{dH_z} \right) H_x \delta H_z \quad (S6)$$

Here, we have expressed χ_c as $d\mu_z/dH_z$. We see from the above equation that it is possible to measure the derivative of the out-of-plane magnetic moment $d\mu_z/dH_z$ with high precision provided H_x is sufficiently large.

Supporting Text:

In-plane vortex penetration $H_{c1} \parallel ab$

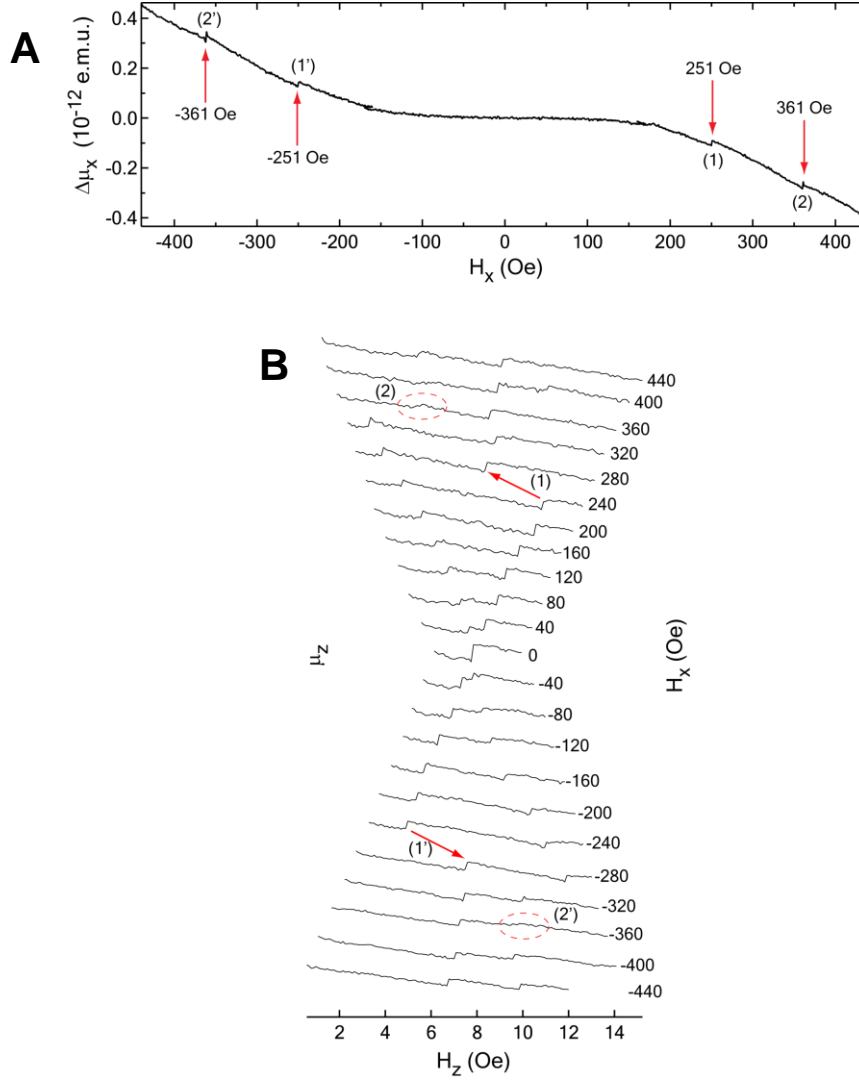


Figure S3: **(A)** In-plane magnetic moment as a function of H_x obtained for the sample presented in Fig. 1 of the main text. Data was obtained for $H_z = 0$ and $T = 0.5$ K. The Meissner response has been subtracted to reveal the steps in the in-plane moment corresponding to the entry of vortices parallel to the direction of the in-plane field (red arrows). **(B)** Out-of-plane magnetic response as a function of H_z and H_x measured at $T = 0.5$ K. The data presented in **(A)** and **(B)** are field-cooled measurements. Accompanying the entry of in-plane vortices, we observe a shift in position (indicated by the red arrows) of the fluxoid transitions, as well as a decrease in the stability region of the HI state.

Here we present a theoretical estimate for $H_{c1} \parallel ab$ for a mesoscopic geometry taking into account the anisotropy in the superconducting response along the c and ab directions. We then compare this estimate to experimental results obtained for the sample presented in the main paper. The energetics of equilibrium vortex entry into a superconductor is affected by the geometry of the sample. In particular, if the magnetic field is applied parallel to the surface of a SC film, H_{c1} is increased above the bulk H_{c1} value (S2). This enhancement in H_{c1} increases as the penetration depth increases relative to the thickness of the film. Roughly speaking, while the energy cost of the vortex core is nearly the same, in thinner films, a vortex saves a smaller amount of magnetic energy.

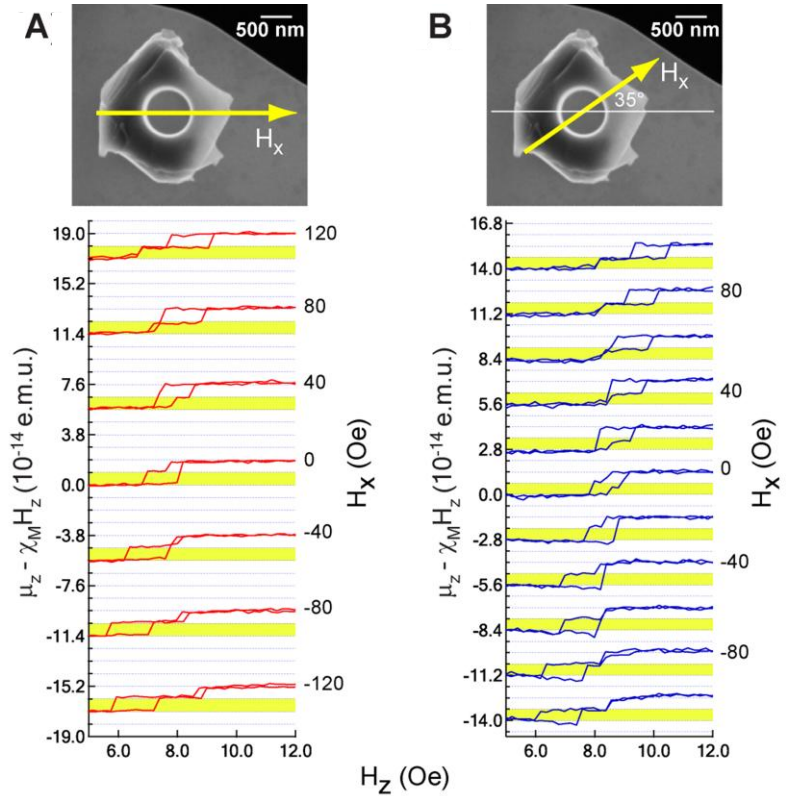
To obtain a theoretical estimate for $H_{c1} \parallel ab$ and $\Delta\mu_x$ (magnitude of the jump in magnetic moment associated with the entry of an in-plane vortex), we consider a superconducting rectangular box of dimension $L_x \times L_y \times h$, where h is the height along the c -axis and the magnetic field is applied along the x -axis. To model the properties of SRO the magnetic response of the box is assumed to be anisotropic with $\gamma_{SC} = \lambda_c(0)/\lambda_{ab}(0) \approx 20$, where $\lambda_c(0)$ and $\lambda_{ab}(0)$ are the zero temperature c -axis and ab -plane penetration depths, respectively (S1). We note that, for the SRO sample in Fig. 1 of the main text, the longest dimension is approximately $1.8 \mu\text{m}$, which is nearly a factor of two smaller than $\lambda_c(0)$; thus, we expect very little screening of H_x . In the limit $L_y \ll \lambda_c$ and $L_y \ll \gamma_{SC}h$, we obtain the following expressions: $H_{c1} \parallel ab = 2\gamma_{SC}\Phi_0 \ln(L_y/(\pi\xi_{ab})) / (\pi L_y^2)$ and $\Delta\mu_x = \Phi_0 L_y \Omega / (32\pi h \lambda_c^2)$, where ξ_{ab} is the in-plane coherence length and Ω is the volume of the superconductor. For a box with $L_y = 1.8 \mu\text{m}$, $h = 0.35 \mu\text{m}$, $\Omega = 0.45 \mu\text{m}^3$ and $\lambda_c = 4.3 \mu\text{m}$, and $\xi_{ab} = 90 \text{ nm}$ —corresponding to the superconducting parameters at $T = 0.4 \text{ K}$, our calculations yield $H_{c1} \parallel ab \approx 150 \text{ Oe}$ and $\Delta\mu_x \approx 4 \times 10^{-14} \text{ e.m.u.}$

We compare this estimate to data obtained for the in-plane moment μ_x shown in Fig. S3; for details on the in-plane moment measurement, see Materials and Methods. For this sample, we find the first vortex entry occurs at $H_{c1} \parallel ab \approx 250 \text{ Oe}$; the measured jump in moment is $\Delta\mu_x \approx 2.2 \times 10^{-14} \text{ e.m.u.}$, both values in reasonable agreement with our estimates. We note that the observed value of $H_{c1} \parallel ab$ for this sample is much higher than the value of $H_{c1} \parallel ab \approx 8 \text{ Oe}$ for bulk SRO (S3) as expected for such mesoscopic geometries.

Effect of rotating the direction of the in-plane magnetic field

To investigate the dependence of the half-integer (HI) state on the direction of the in-plane magnetic field, we applied the in-plane magnetic field H_x along two directions rotated by 35° (see Fig. S4). Our goal was to verify whether the direction H_x is important in the half-integer fraction observed in the magnetization steps accompanying fluxoid transitions as well as the dependence on the stability region of the HI state (i.e., the range of H_z for which the HI state is the equilibrium state) on the magnitude of the in-plane field. We find that the half-step features persist and, furthermore, that the field-dependence of the stability region is not strongly influenced by the direction of the in-plane field.

Figure S4: (A-B) In-plane field dependence of the $n = 0 \rightarrow n = 1$ transition measured at $T = 0.5$ K—the curves have been offset for clarity. The data were obtained by zero field cooling the sample and performing a cyclic field sweep starting from $H_z = 0$. To vary the direction of H_x , the cantilever was rotated in the xy -plane, yielding the data shown in (B). The data shown in (A) and (B) were obtained in separate experimental runs. To quantify the change in moment associated with the observed transitions, we obtain χ_M by fitting to the linear Messiner response between $-8 \text{ Oe} < H_z < 8 \text{ Oe}$ for the $H_x = 0$ data and then subtract $\chi_M H_z$ from the data measured at different values of H_x .



Possible scenarios for the HI state

In this supplemental section we discuss three possible scenarios for the theoretical interpretation of the HI state: A kinematic spin polarization scenario in a half-quantum vortex state, a π -junction scenario, and a “wall vortex” scenario. We argue that the first scenario is more consistent with the magnitude of the observed in-plane field dependence of the HI state, whereas the last two scenarios are not consistent with our observations.

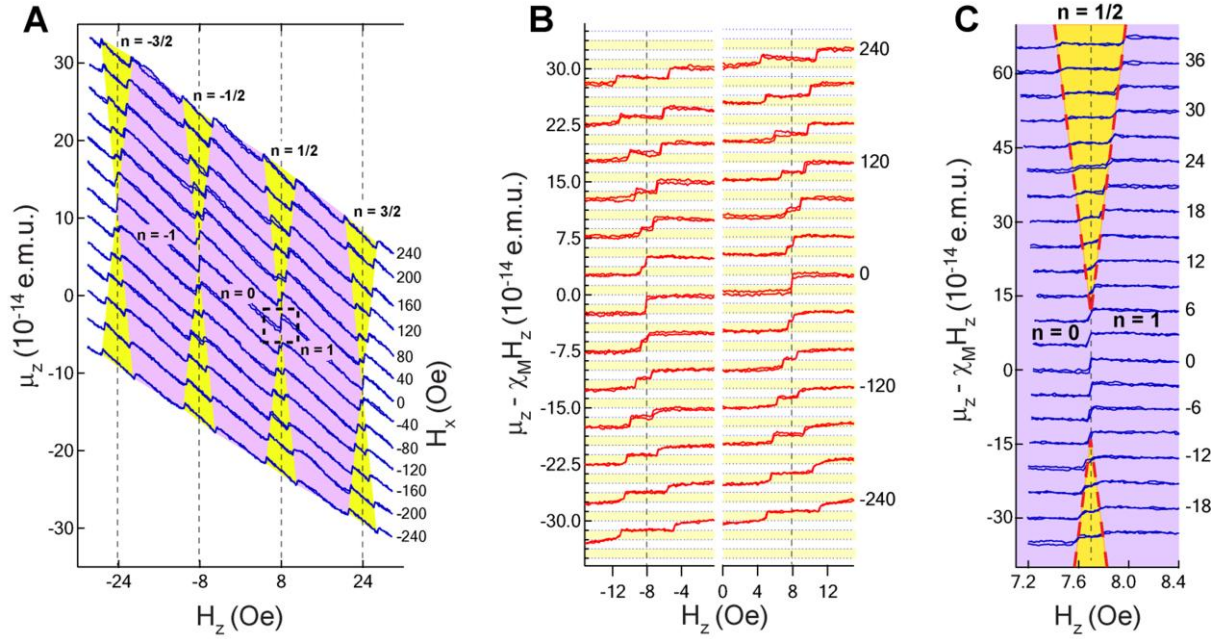


Figure S5: Plots showing zero-field-cooled data obtained at $T = 0.6$ K for the sample shown in Fig. 1 of the main text. The data shown in (A) represent the full magnetic response of the particle. The purple shaded regions indicate IF states, whereas the yellow shading indicates the regions in which the HI state is stable. (B) The data shown in (A) after subtraction of the linear Meissner response. (C) Data taken near the $n = 0 \rightarrow n = 1$ transition for the range of in-plane fields indicated by the dashed box in (A)—the Meissner response has been subtracted from each curve. The data shown in (B-C) have been offset for clarity by an amount proportional to H_x .

Based on the measurements of the SRO samples, we construct the following total Gibbs free energy (S4) which captures the main features of the observed magnetic response:

$$G(\mathbf{H}, n) = E_0 (n - H_z/\Delta H_z)^2 - \bar{\chi} H_z^2/2 + E_{\text{HI}} - \boldsymbol{\mu}_{\text{HI}} \cdot \mathbf{H}, \quad (\text{S7})$$

where n can be integral or half-integral (i.e., HI states) (cf. Fig. S5A), and the parameters E_0 and $\bar{\chi}$ are expressible via measured quantities: $E_0 = \Delta\mu_z \Delta H_z/2$ and $\bar{\chi} = \chi_M + \Delta\mu_z/\Delta H_z$. Note that to account for the growth of the stability region of the HI states with in-plane field we have included two terms that are only nonzero in HI states: $-\boldsymbol{\mu}_{\text{HI}} \cdot \mathbf{H}$, where $\boldsymbol{\mu}_{\text{HI}}$ is a magnetic moment that exists only in the HI state and points in the direction of the in-plane field; and a field-independent constant contribution E_{HI} . From Eq. (S7), we can relate the model parameters to the growth in the stability region of the HI state as a function of H_x : $\delta H_z = 4 \mu_{\text{HI}}(H_x - H_{x,\text{min}})/\Delta\mu_z$ (for $H_x > H_{x,\text{min}}$) and $E_{\text{HI}} = E_0/4 + \mu_{\text{HI}} H_{x,\text{min}}$. For the data shown in Fig. S5, we find $E_0 \approx 0.1$ eV, $\Delta\mu_z \approx 2 \times 10^{-14}$ e.m.u., $\mu_{\text{HI}} \approx 1 \times 10^{-16}$ e.m.u., and $E_{\text{HI}}/E_0 \approx 0.26$. We note that the value of μ_{HI} obtained is roughly 200 times smaller than the magnitude of the magnetic moment measured for an in-plane vortex ($\Delta\mu_x = 2.2 \times 10^{-14}$ e.m.u.).

The kinematic spin polarization scenario in a half-quantum vortex state

As previously stated, in the linear regime—provided the ESP description holds—we expect the height of the steps in the magnetic moment that occur at the transition to the HF state to be half of those that occur at IF transitions. A robust halving of the magnetization steps, which follows naturally from the theoretical framework of HQVs, is what we observe throughout the range of fields and temperatures studied. Perhaps the most intriguing observation is of an in-plane magnetic moment $\boldsymbol{\mu}_{\text{HI}}$ in the HI state. While the origin of this moment is, as yet, unknown, recent work by Vakaryuk and Leggett (S5) finds that a kinematic spin polarization $\boldsymbol{\mu}_s^{\text{kin}}$ can develop in the HQV state, as a result of the velocity mismatch between the $|\uparrow\uparrow\rangle$ and $|\downarrow\downarrow\rangle$ superfluid components. While, theoretically, the magnitude of $\boldsymbol{\mu}_s^{\text{kin}}$ depends on the distribution of both charge and spin currents, we estimate it to be of the same order of magnitude as the experimental value of $\mu_{\text{HI}} \approx 1 \times 10^{-16}$ e.m.u. (see the next section of the SOM for more details).

To complete the interpretation of the experimental data, described by Eq. (S7), within the framework of HQVs, we consider two additional factors that are primarily responsible for the

free-energy difference between the HF and IF states captured by the term E_{HI} in Eq. (S7): one arises from the presence of spin currents; the other from “spin-orbit” interactions (S6), which depend on the orientation of \mathbf{d} with respect to the internal Cooper-pair angular momentum for the full and half quantum vortex states. The contribution from the spin currents is determined by their spatial distribution, and is proportional to the spin superfluid density ρ_{sp} (S7-S8). To evaluate the contribution of spin-orbit interactions, both the orientation of \mathbf{d} and the spin-orbit coupling strength are needed—neither have been experimentally determined. Theoretically, there are several models for the order parameter of SRO which predict distinct orientations for \mathbf{d} (see e.g. (S1, S9-S10)). Our interpretation of μ_{HI} as being caused by a spin polarization implies that the ESP axis should be in the direction of the in-plane field for the range of fields studied.

The π -junction scenario

Under certain circumstances, there can exist crystal grain boundary Josephson junctions within the sample that can shift the total phase winding by π (S11). However, our samples are fabricated from high quality single crystals, and thus it is unlikely that they contain the grain boundaries and orientations necessary to realize a π -junction. Moreover, even assuming that the presence of a π -junction, such as in (S11), its impact would be to shift the values of the out-of-plane magnetic field at which the fluxoid transitions occur by $\Delta H_z/2$. We do not find evidence of such a shift in our data. Furthermore, the π -junction scenario would produce a jump in magnetic moment identical to that for a conventional full-quantum vortex. It would not lead to the half-height jumps of the magnetic moment. Therefore, it seems implausible that such a scenario is relevant to our observations.

The wall vortex scenario

We refer to a wall vortex (WV) as any state where a vortex penetrates through the volume of the sample. In general, a transition between a WV state and the $n = 0$ integer fluxoid state will correspond to a change in the particle’s magnetic moment $\Delta\mu_{\text{WV}}$. Thus, to interpret the HI state as a WV state, $\Delta\mu_{\text{WV}}$ would need to be consistent with the observed value of $(\Delta\mu_z/2)\hat{\mathbf{z}} + \mu_{\text{HI}}$. For the experimental particles where the HI state is observed, the local superconducting properties are not known in detail. Therefore it is difficult to constrain the possible forms of WV states. However, we can make the following general observations: (i) For the ob-

served in-plane vortices corresponding to fields $H_x \geq 250$ Oe (Fig. S3), the magnitude of the in-plane component of $\Delta\mu_{WV}$ is approximately 200 times larger than μ_{HI} . Thus, the HI state is not a simple generalization of the observed in-plane WV state. (ii) The z-axis component of $\Delta\mu_{WV}$ can be any fraction of $\Delta\mu_z$ and is not generically $\Delta\mu_z/2$. (iii) In general, we would expect the location/orientation of wall vortices to vary with the magnitude and direction of the applied field. Hence, we would expect multiple fractional steps in the magnetic moment; these steps correspond to transitions involving various WV states. (iv) Given the geometric asymmetry of our samples, we would also expect that the component of $\Delta\mu_{WV}$ along the in-plane field to vary with the direction of the in-plane field. Consequently, the stability region of the WV state should be affected by the direction of the in-plane field. However, over the range of fields studied for the SRO particle shown in Fig. 1 of the main text, we find that the stability region of the HI feature is not influenced by the direction of the in-plane field (Fig. S4). Given these considerations we conclude that to formulate a wall vortex scenario consistent with the observed properties of the HI state would require a fine tuned set of assumptions, and is thus unlikely.

Effect of kinematic spin polarization on the stability of HQV state

As pointed out in (S5), the velocity mismatch between $|\uparrow\uparrow\rangle$ and $|\downarrow\downarrow\rangle$ spin components of an ESP superfluid in the HQV state gives rise to an effective Zeeman field B_{eff} which, in thermal equilibrium, produces a kinematic spin polarization in addition to that caused by the Zeeman coupling to the external field. Such kinematic spin polarization is absent in the full vortex state where the velocities of $|\uparrow\uparrow\rangle$ and $|\downarrow\downarrow\rangle$ components are the same. The goal of this section is to argue that the coupling between the kinematic spin polarization and the external field can account for the experimentally observed growth of the stability region of half-integer steps. The detailed calculation of the effect of the kinematic spin polarization on the stability of HQVs will be given elsewhere.

Generalizing results of ref. (S5) for an ESP superconductor of arbitrary geometry the effective Zeeman field in the HQV state becomes a local vector which points along the ESP axis and its magnitude is given by

$$B_{eff}(\mathbf{r}, \mathbf{H}) = -\frac{m^*}{g_s \mu_B} \left(1 + \frac{F_1}{3} + \frac{Z_1}{12}\right) \mathbf{v}_s(\mathbf{r}, \mathbf{H}) \cdot \mathbf{v}_{sp}(\mathbf{r}) \quad (\text{S8})$$

where m^* is the Fermi-liquid mass of the charge carriers and g_s is their gyromagnetic ratio. Fermi-liquid parameters F_1 and Z_1 describe renormalization of charge and spin currents respectively; the notation for Fermi liquid parameters is the same as in (S7). In the expression (S8) \mathbf{v}_s and \mathbf{v}_{sp} are the local charge and spin superfluid velocities respectively; the superfluid velocity v_s which describes motion of charges in the system couples to the applied field \mathbf{H} .

In our experimental setup the applied field \mathbf{H} has both in-plane (H_x) and c -axis (H_z) components. However, because of the large superconducting and shape anisotropies of the sample, the measured magnetic response, and hence the current distribution, is dominated by the c -axis field. Assuming that the ESP axis lies in the ab plane, the Gibbs potential of full and half-quantum vortices can be written as

$$G^{FQV}(\mathbf{H}) = G_0^{FQV}(H_z) - \frac{1}{2} \chi_s \int \frac{d^3 \mathbf{r}}{\Omega} H_x^2 \quad (\text{S9})$$

$$G^{HQV}(\mathbf{H}) = G_0^{HQV}(H_z) - \frac{1}{2} \chi_s \int \frac{d^3 \mathbf{r}}{\Omega} \{H_x - B_{eff}(\mathbf{r}, H_z)\}^2$$

where only spin-polarization parts of the energies have been explicitly written. Here, χ_s and Ω are the spin susceptibility and sample volume, respectively. The region of the thermodynamic stability of the HQV as a function of the applied field \mathbf{H} is determined by equating the above Gibbs potentials which leads to the following equation

$$\chi_s H_x \int \frac{d^3 \mathbf{r}}{\Omega} B_{eff}(\mathbf{r}, H_z) = \delta G(H_z) \quad (\text{S10})$$

It should be emphasized that the dependence on the in-plane field H_x in the above equation enters only linearly through the l.h.s., as explicitly indicated, while all other energy contributions are gathered on the r.h.s. and are denoted as $\delta G(H_z)$.

To analyze the dependence of the c -axis field stability region of the HQV on the in-plane field H_x as implicitly determined by Eqn. (S10) we note that the kinematics of charge and spin currents favors the stability region to be located around the field corresponding to the transition between full vortex states. Denoting this field as $H_z^{(0)}$ and expanding both $B_{eff}(\mathbf{r}, H_z)$ and $\delta G(H_z)$ in its neighborhood we obtain that the c -axis field stability region of HQV depends linearly on the in-plane field with the slope given by

$$\left. \frac{dH_z}{dH_x} \right|_{FQV \rightarrow HQV} = \frac{\chi_s B_{eff}}{\Delta M} \zeta \quad (S11)$$

where ΔM is the magnetization jump between full and half-quantum vortex states as derived from $\delta G(H_z)$; parameters ζ and B_{eff} are defined below. Denoting the characteristic size of the sample as R , the dimensionless parameter ζ is given by

$$\zeta \equiv \left[\frac{\hbar}{2m^*R} \right]^{-2} \int \frac{d^3\mathbf{r}}{\Omega} \mathbf{v}_s(\mathbf{r}, H_z^{(0)}) \cdot \mathbf{v}_{sp}(\mathbf{r}) \quad (S12)$$

and characterizes the overlap of the charge and spin currents. Although the exact distributions of both currents for our sample are unknown, the important observation is that for a mesoscopic sample with dimensions comparable to the London penetration depth the overlap integral which determines ζ need not be small.

The other parameter in Eqn. (S12) is a constant field B_{eff} defined as

$$B_{eff} \equiv \frac{1}{2g_s} \left[1 + \frac{Z_1/12}{1 + F_1/3} \right] \frac{\phi_0}{\pi R^2} \quad (S13)$$

Given the free-electron value of the gyromagnetic ratio $g_s = 2$, the size of our sample and the assumption that Fermi liquid parameter Z_1 is small (as it is for ^3He) B_{eff} is estimated to be of order 5 G. The crucial observation is that the magnitude of B_{eff} depends substantially on the size of the sample.

It is convenient to transform the overlap integral in ζ to a form which involves a surface integral. Given that (i) the spin superfluid velocity \mathbf{v}_{sp} is described by a potential flow, and (ii) superfluid velocity \mathbf{v}_s is proportional to the superconducting current density, one obtains the following alternative form of ζ :

$$\zeta = \frac{m^*R}{\hbar} \frac{\lambda_L^2}{\phi_0} \int \frac{R d^2\mathbf{S}}{\pi\Omega} \cdot (\mathbf{H} \times \mathbf{v}_{sp}) \quad (S14)$$

where \mathbf{H} is the total magnetic field on the surface of superconductor. However, the condition of the potentiality of the spin superflow leads to the conclusion that a part of \mathbf{H} which is constant and uniform (e.g. the applied field) does not contribute to the value of ζ so that the field \mathbf{H} in Eqn. (S14) can be treated as the one generated by the superconductor only.

To obtain an estimate of ζ we consider a doughnut-shaped superconducting sample with the mean and cross-section radii denoted as R and r , respectively. For this geometry, the magnetic field on the surface is given by $2M/\pi R^2 r$, where M is the magnetic moment of the doughnut,

and, provided the rotation of the \mathbf{d} is uniform, the average value of the spin current in the HQV state is given by $\hbar/4m^*R$. This leads to the following expression for ζ :

$$\zeta \approx 8\pi^2 \frac{\lambda_L^2 M}{\phi_0 \Omega} \quad (\text{S15})$$

The magnetic moment M , which is determined by the applied field H_z , depends also on the geometry of the sample and on the value of the penetration depth. For a small sample, the latter dependence can be factored out and M can be approximated by $M \approx H_z \Omega R^2 / 2\pi \lambda_L^2$ which gives $\zeta \sim 1$ for the values of the applied fields typical for our experiment.

We can now estimate the slope of the transition line between the full and half quantum vortex states as given by Eqn. (S11) and also the magnitude of the kinematic spin polarization which follows from it. Using the estimates for B_{eff} and ζ obtained above, $\Delta M \approx 10^{-14}$ e.m.u and $\chi_S \approx 2 \times 10^{-17} \text{ cm}^3$, which is obtained from the molar spin susceptibility of SRO (i.e. 10^{-3} e.m.u/mol (S12)) and the volume of the sample, we find $\left. \frac{dH_z}{dH_x} \right|_{FQV \rightarrow HQV} \approx 0.01$ and $\mu_S^{kin} \approx 10^{-16}$ e.m.u., in agreement with the experimentally observed value.

Edge currents from chiral domains

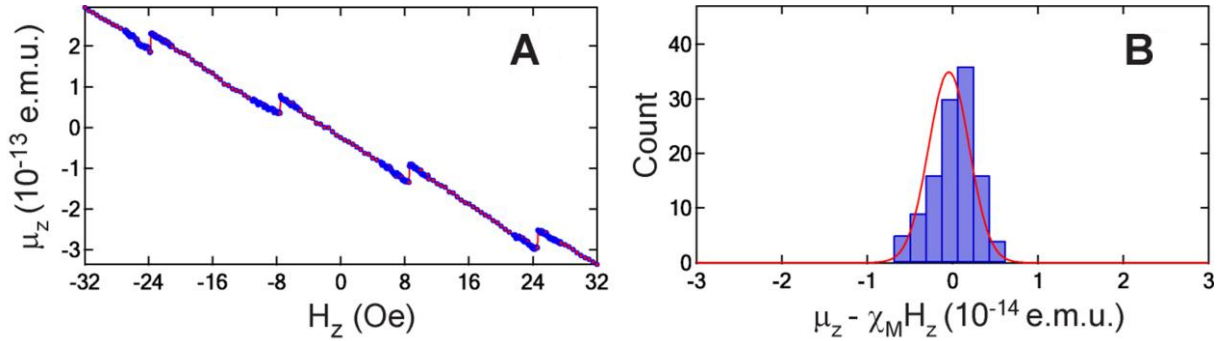
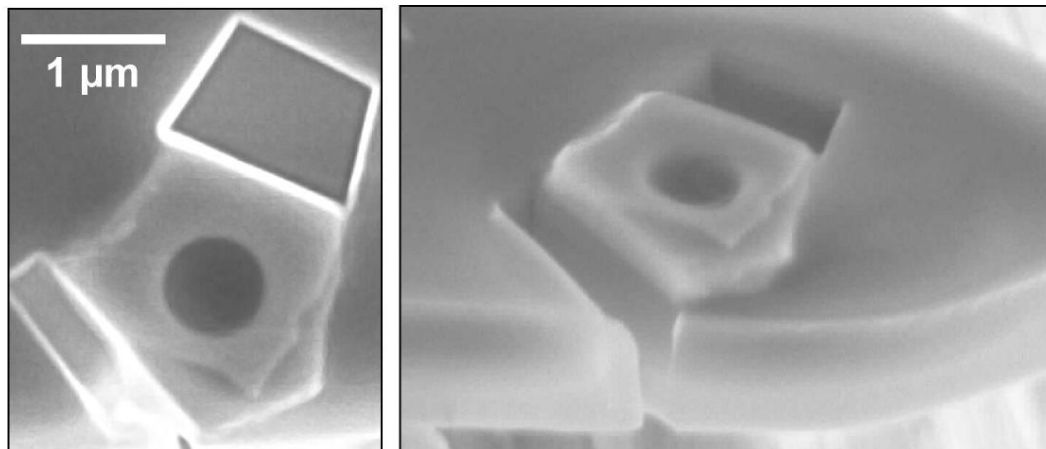


Figure S6: (A) Field-cooled data obtained at $T = 0.4$ K for $H_x = 0$. To quantify the fluctuations in the magnetic moment μ_z , we subtract the Meissner response and histogram the difference $\mu_z - \chi_M H_z$. The histogram shown in (B) represent the fluctuations for field-cooled data between $-8 \text{ Oe} < H_z < 8 \text{ Oe}$; the standard deviation fluctuations is $\sigma_z = 2.5 \times 10^{-15}$ e.m.u..

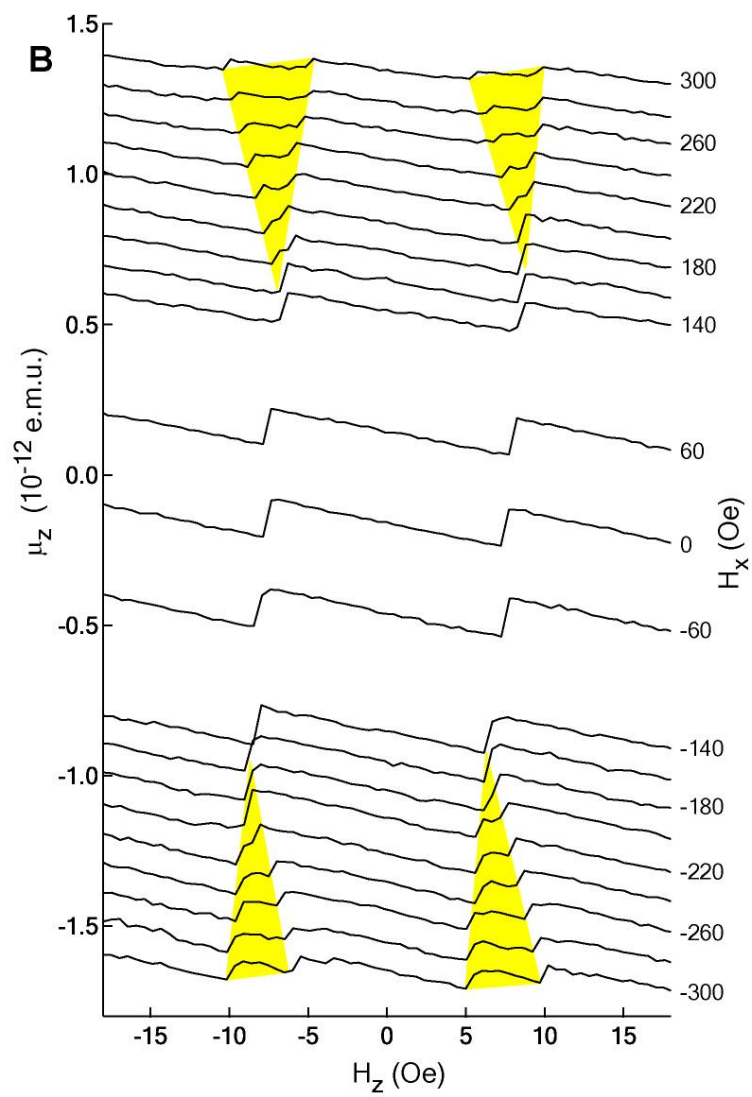
To compare the in-plane orientation of the ESP axis that our interpretation of the data implies with the orientation proposed in the literature (*S1*), we note that of the five possible unitary states that lack symmetry required nodes, only the chiral states, which have the schematic form $\hat{\mathbf{d}} = \hat{z}(p_x \pm i p_y)$, have their ESP axis in-plane. Such chiral states have been predicted to carry spontaneous edge-currents of magnitude 5.6×10^{-6} A per layer (*S13-S14*). If the sample has a single chiral domain then, together, the chiral currents and the Meissner screening currents, would produce an additional magnetic moment along the c-axis, of order $\pm 10^{-12}$ e.m.u. However, to within the noise resolution of the experiment, the field-cooled magnetization curve of Fig. S6A shows no signature of a zero-field moment, which limits its observed value to less than 2.5×10^{-15} e.m.u. Several effects may account for this discrepancy: (i) a reduction of the edge currents (see e.g. (*S10, S15*)), (ii) the presence of multiple domains (*S16*), or (iii) insufficient thermalization of the particle during the field-cooling procedure. To resolve this discrepancy, a more systematic study is needed. We emphasize, however, that the existence of HQVs requires only ESP. Thus, even if we accept the basic idea that the observation of an HI state would infer the existence of an (underlying) HF state, further reasoning is required to pin down the precise form of the superconducting state.

SRO Sample #2

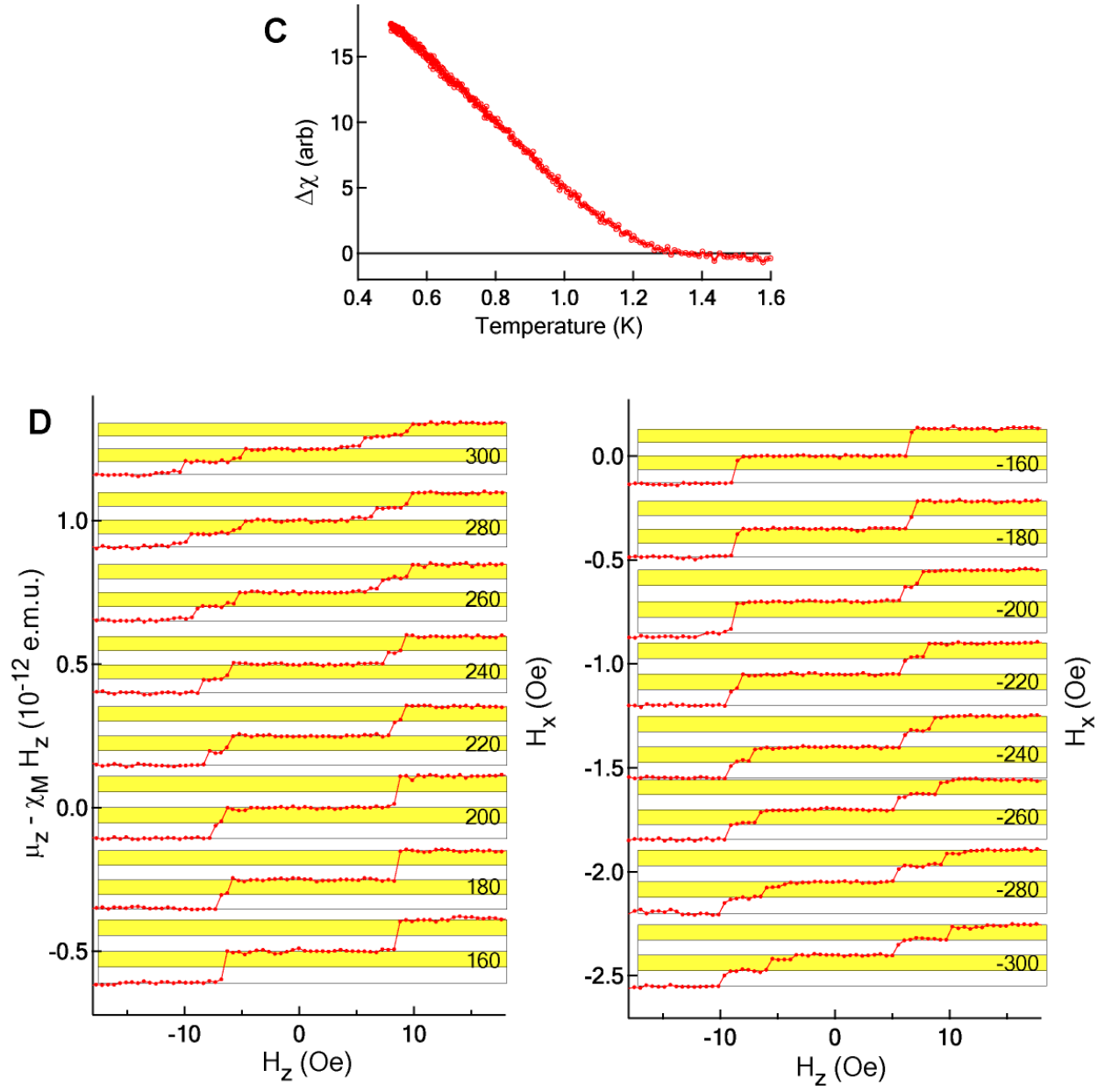
A



B



SRO Sample #2



SRO Sample #2

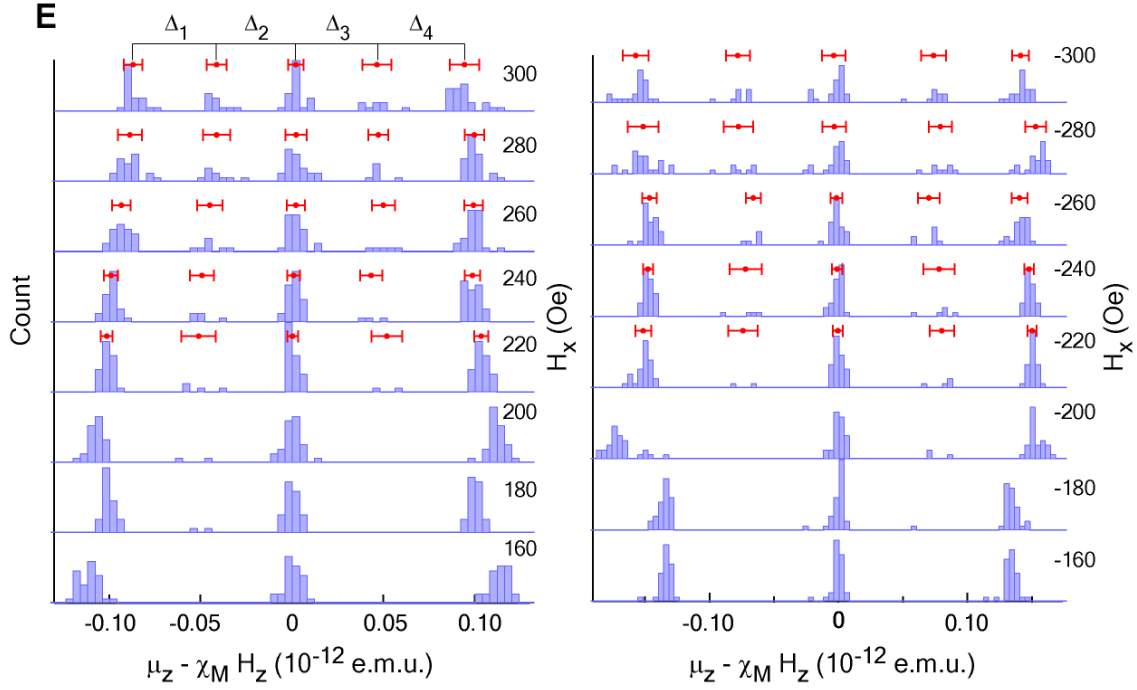
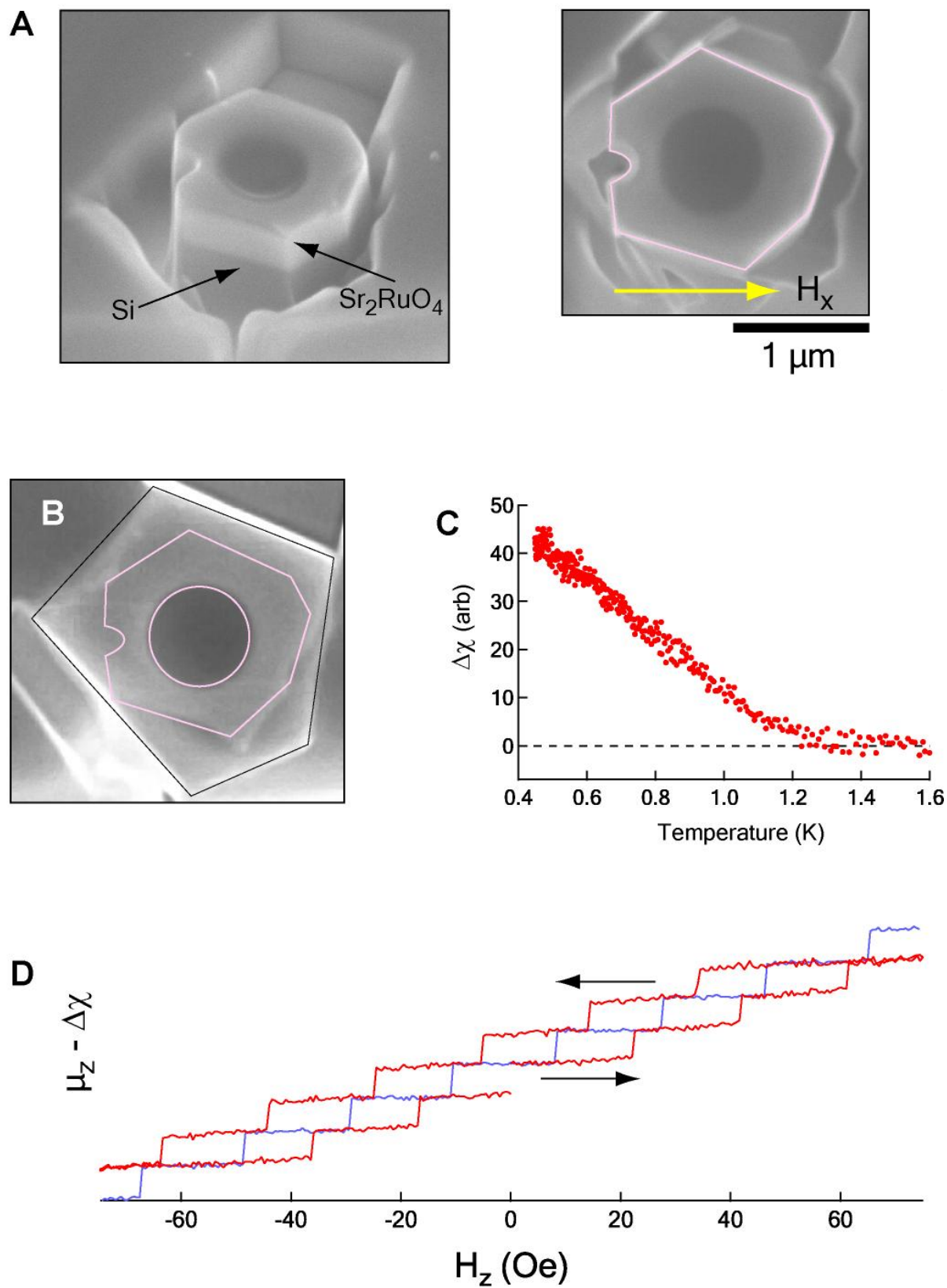


Figure S7: (A) SEM of a 0.35- μm thick annular SRO particle with a 0.75- μm diameter hole. The SRO particle is shown glued to a silicon cantilever, the notches in the cantilever are a result of the focused ion beam shaping of the particle. To obtain the equilibrium magnetic response, the particle is field cooled at each value of the applied field. (B) Equilibrium data obtained at $T = 0.8\text{ K}$; each curve has been offset for clarity. (C) The susceptibility of the particle as a function of temperature. (D) Meissner-subtracted data. (E) Histograms of the Meissner-subtracted data.

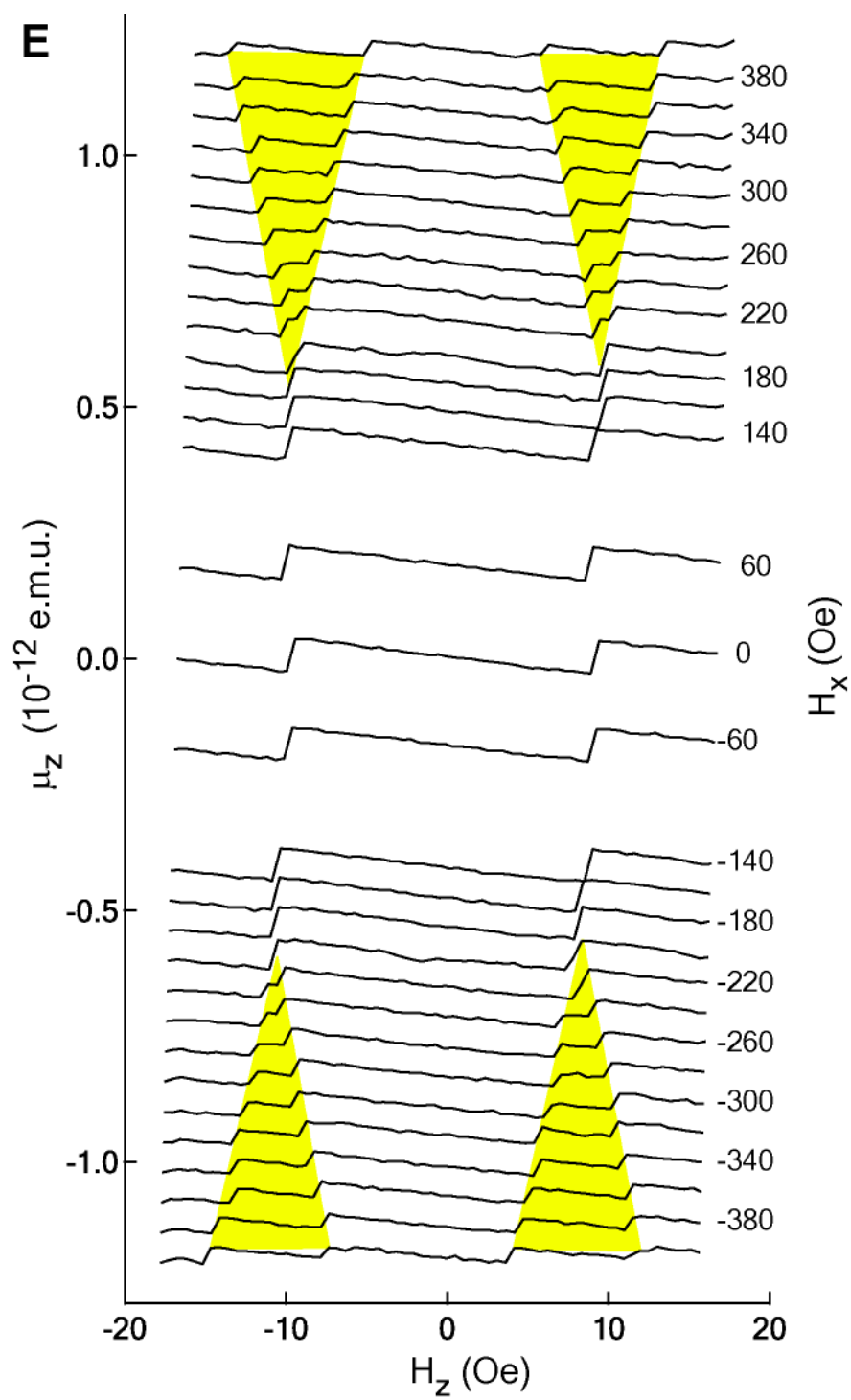
H_x (Oe)	$\Delta_1/(\Delta_1 + \Delta_2)$	$\Delta_3/(\Delta_3 + \Delta_4)$
300	0.51 ± 0.06	0.48 ± 0.08
280	0.52 ± 0.07	0.46 ± 0.06
260	0.51 ± 0.06	0.49 ± 0.06
240	0.50 ± 0.05	0.43 ± 0.05
220	0.49 ± 0.07	0.50 ± 0.06
-220	0.51 ± 0.06	0.53 ± 0.05
-240	0.52 ± 0.06	0.53 ± 0.06
-260	0.56 ± 0.04	0.50 ± 0.05
-280	0.50 ± 0.07	0.53 ± 0.06
-300	0.52 ± 0.06	0.53 ± 0.06
	$\langle \Delta_1/(\Delta_1 + \Delta_2) \rangle$	$\langle \Delta_3/(\Delta_3 + \Delta_4) \rangle$
	0.51 ± 0.02	0.50 ± 0.02

Table S1: The calculated fractional step heights for the data shown in Fig. S7E. The average value of a given fractional step is indicated by the quantity $\langle \dots \rangle$.

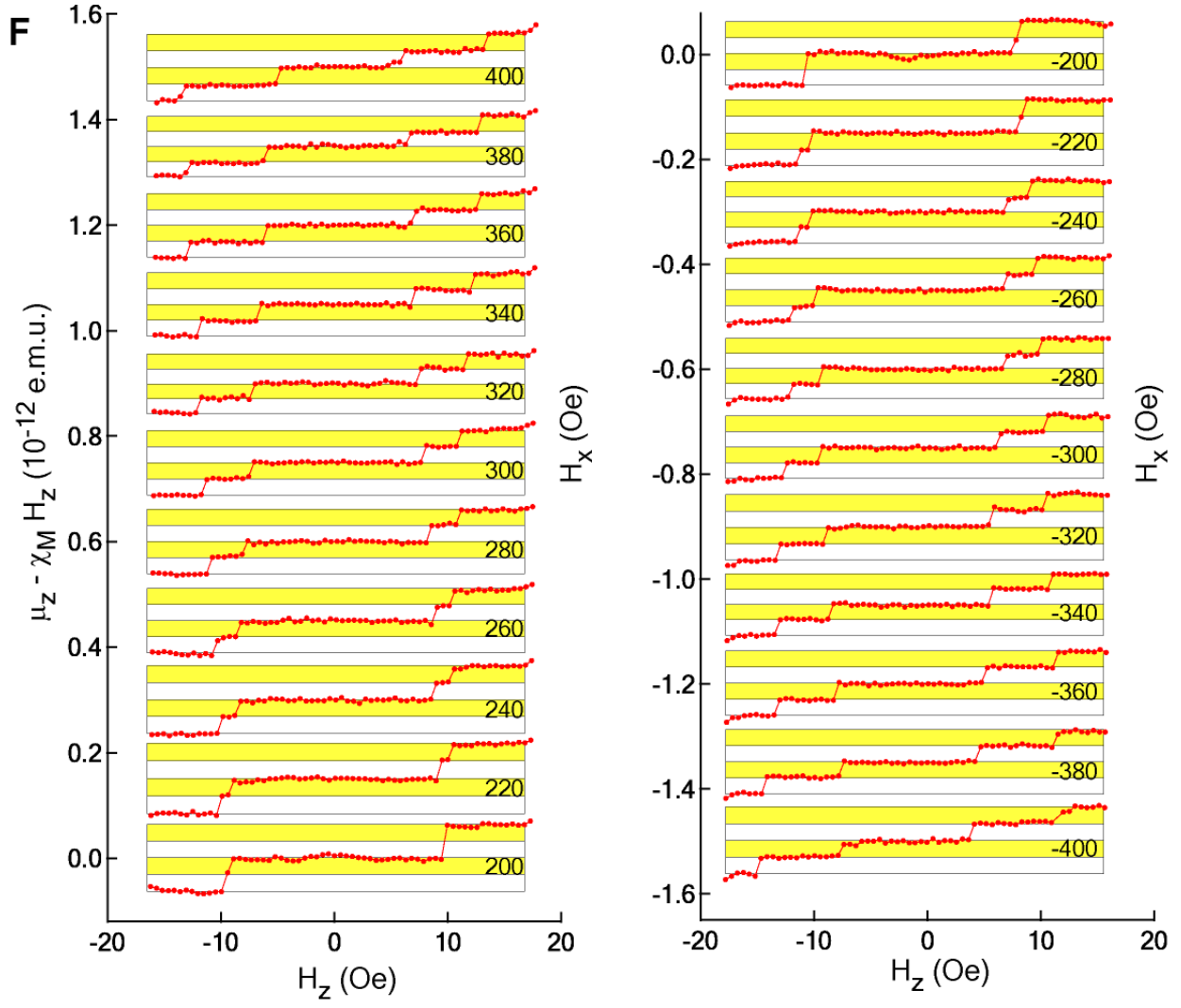
SRO Sample #3



SRO Sample #3



SRO Sample #3



SRO Sample #3

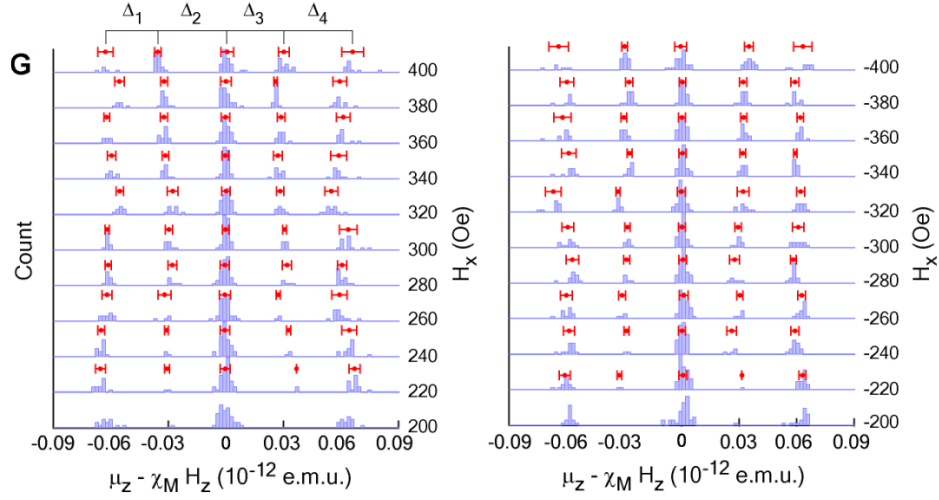


Figure S8: (A) SEM of the sample shown in Fig. S13 after being reshaped by the focused ion beam. (B) Comparison before-and-after reshaping the particle. The black outline indicates the boundary of the sample as it appears in Fig. S7A; the purple outline indicates the boundary after reshaping; the overall sample volume has been reduced to 44% of its initial volume after the reshaping. (C) The susceptibility of the particle after reshaping as a function of temperature. (D) The Meissner-subtracted equilibrium (blue curve) and zero-field-cooled data (red curve) obtained for $H_x = 0$ at $T = 0.5$ K. We note, although the sample dimensions have been reduced considerably, the transitions are still highly hysteretic, indicating that the ring does not possess a weak link. (E) Equilibrium data obtained at $T = 0.5$ K; each curve has been offset for clarity. (F) The Meissner-subtracted data. (G) Histograms of the Meissner-subtracted data.

H_x (Oe)	$\Delta_1/(\Delta_1 + \Delta_2)$	$\Delta_3/(\Delta_3 + \Delta_4)$
400	0.43 ± 0.05	0.45 ± 0.06
380	0.42 ± 0.04	0.44 ± 0.04
360	0.48 ± 0.03	0.47 ± 0.04
340	0.47 ± 0.03	0.46 ± 0.05
320	0.50 ± 0.04	0.51 ± 0.04
300	0.52 ± 0.03	0.48 ± 0.04
280	0.55 ± 0.04	0.53 ± 0.04
260	0.49 ± 0.05	0.47 ± 0.04
240	0.53 ± 0.03	0.51 ± 0.04
220	0.53 ± 0.03	0.55 ± 0.03
-220	0.46 ± 0.03	0.49 ± 0.02
-240	0.51 ± 0.03	0.44 ± 0.04
-260	0.48 ± 0.04	0.48 ± 0.03
-280	0.49 ± 0.04	0.47 ± 0.04

-300	0.52 ± 0.03	0.48 ± 0.04
-320	0.51 ± 0.04	0.52 ± 0.04
-340	0.54 ± 0.04	0.53 ± 0.02
-360	0.52 ± 0.04	0.52 ± 0.03
-380	0.54 ± 0.04	0.54 ± 0.03
-400	0.54 ± 0.05	0.56 ± 0.05
	$\langle \Delta_1/(\Delta_1 + \Delta_2) \rangle$	$\langle \Delta_3/(\Delta_3 + \Delta_4) \rangle$
	0.50 ± 0.01	0.50 ± 0.01

Table S2: The calculated fractional step heights for the data shown in Fig. S8G. The average value of a given fractional step is indicated by the quantity $\langle \dots \rangle$.

SRO Sample #4

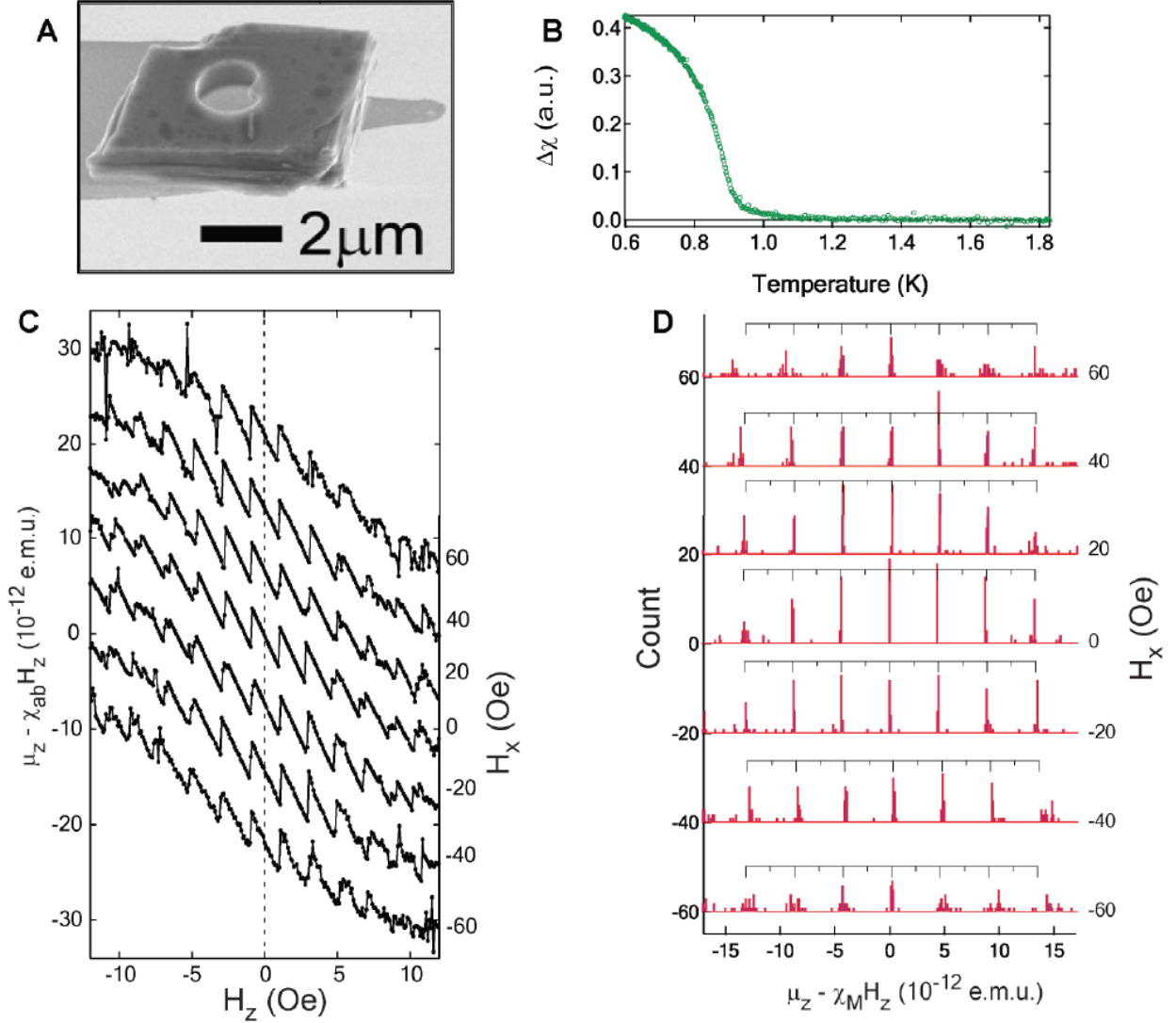


Figure S9: (A) SEM of a $6\ \mu\text{m} \times 4\ \mu\text{m} \times 1.6\ \mu\text{m}$ (thick) annular SRO particle with a $1.7\ \mu\text{m}$ diameter hole; the particle is shown attached to the tip of a silicon cantilever. (B) The susceptibility of the particle as a function of temperature. (C) Field-cooled data obtained at $T = 0.5\ \text{K}$ for values of the in-plane magnetic field between $-60\ \text{Oe}$ to $60\ \text{Oe}$. Each curve has been offset for clarity. (D) Histograms of the Meissner-subtracted data. The histograms represent data for the $n = -3$ to $n = 3$ fluxoid transitions. As a guide to the eye, we have placed a scale bar above each histogram, where the major ticks represent the values of the magnetic moment corresponding to the integer fluxoid states of the hole.

NbSe₂ sample

For comparison, we have studied the magnetic response of an annular conventional superconductor of similar size to the SRO particle presented in the main text. We chose the s-wave superconductor NbSe₂ because, like SRO, it is a layered compound that exhibits an anisotropic superconducting response; the effective mass anisotropy in NbSe₂ is $(\lambda_c/\lambda_{ab}) \approx 4$. The c -axis penetration depth $\lambda_{ab} = 0.15 \mu m$ is comparable to that of SRO.

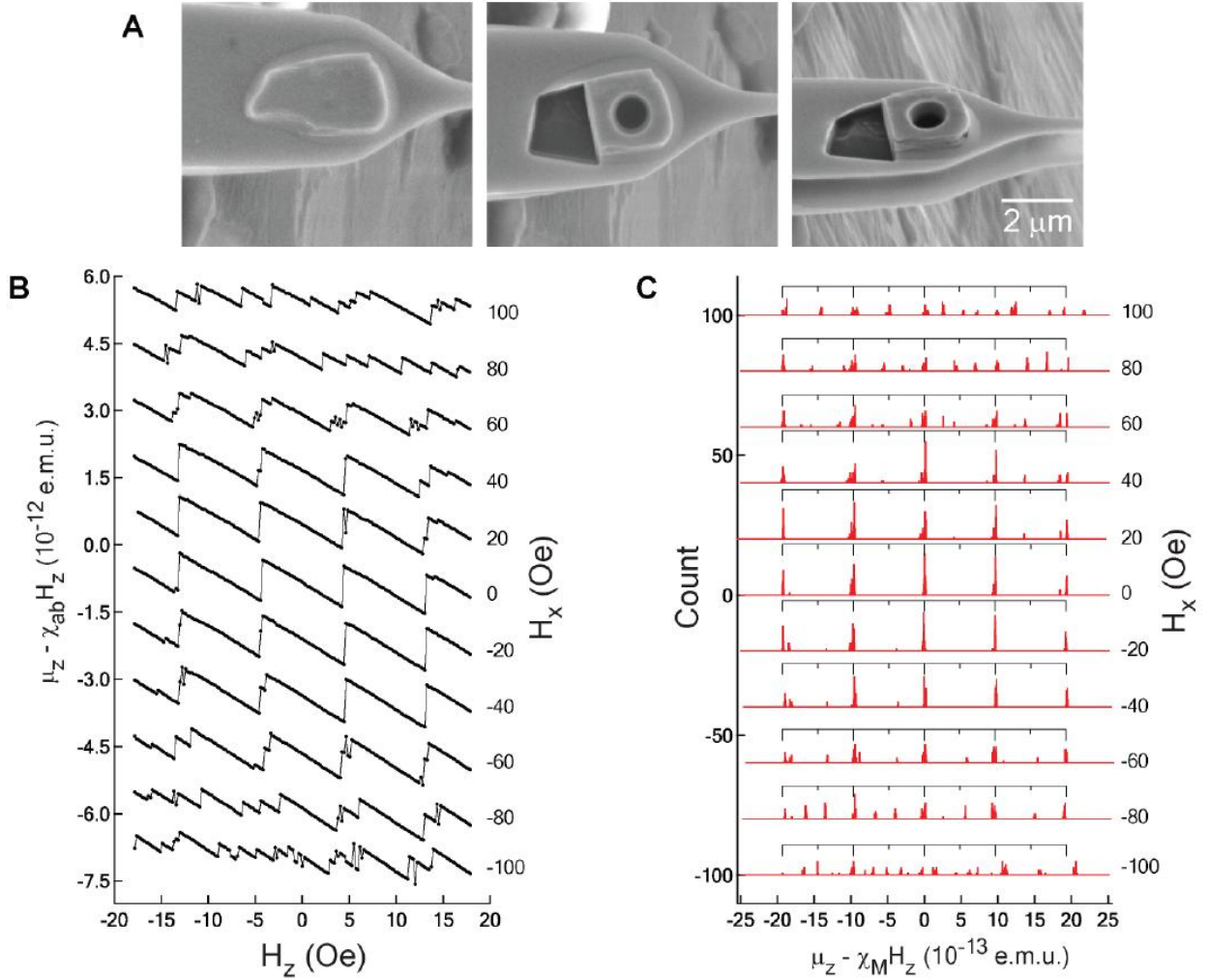


Figure S10: (A) SEM of a $2 \mu m \times 2 \mu m \times 0.3 \mu m$ (thick) annular NbSe₂ particle with a $1.0 \mu m$ diameter hole is shown in central and right hand panels; the image on the left shows the particle after being glued to the tip of a silicon cantilever prior to being shaped by the focused ion beam. The critical temperature of the annular particle was determined to be $T_c = 7.2$ K. (B) Field-cooled data obtained at $T = 6.0$ K for values of the in-plane magnetic field between -100 Oe to 100 Oe. Each curve has been offset for clarity. (C) Histograms of the Meissner-subtracted data;

histograms have been offset for clarity. As a guide to the eye, we have placed a scale bar above each histogram, where the major ticks represent the values of the magnetic moment corresponding to the integer fluxoid states of the hole.

Supporting References and Notes

- S1. A. P. Mackenzie, Y. Maeno, The superconductivity of Sr_2RuO_4 and the physics of spin-triplet pairing. *Rev. Mod. Phys.* **75**, 657 (2003).
- S2. A. A. Abrikosov, On the lower critical field of thin layers of superconductors of the 2nd group. *JETP* **19**, 988 (1964).
- S3. K. Yoshida, Y. Maeno, S. Nishizaki, T. Fujita, Anisotropic superconductivity of Sr_2RuO_4 . *Physica C* **263**, 519 (1996).
- S4. L. D. Landau, E. M. Lifshitz, L. P. Pitaevskii, *Electrodynamics of continuous media*. Course of theoretical physics (Pergamon, New York, ed. 2, 1984), pp. 116.
- S5. V. Vakaryuk, A. J. Leggett, Spin polarization of half-quantum vortex in systems with equal spin pairing. *Phys. Rev. Lett.* **103**, 057003 (2009).
- S6. In ^3He such coupling arises from the dipole interaction between ^3He atoms, while in SRO it may arise both from single-particle spin-orbit effects and from electron-electron interactions.
- S7. A. J. Leggett, A theoretical description of the new phases of liquid ^3He . *Rev. Mod. Phys.* **47**, 331 (1975).
- S8. S. B. Chung, H. Bluhm, E.-A. Kim, Stability of half-quantum vortices in p_x+ip_y superconductors. *Phys. Rev. Lett.* **99**, 197002 (2007).
- S9. Y. Yoshioka, K. Miyake, Pairing mechanism and anisotropy of d-vector of spin-triplet superconductor Sr_2RuO_4 . *J. Phys. Soc. Jpn.* **78**, 074701 (2009).

- S10. S. Raghu, A. Kapitulnik, S. A. Kivelson, Hidden quasi-one-dimensional superconductivity in Sr_2RuO_4 . *Phys. Rev. Lett.* **105**, 136401 (2010).
- S11. C. C. Tsuei *et al.*, Pairing symmetry and flux quantization in a tricrystal superconducting ring of $\text{YBa}_2\text{Cu}_3\text{O}_{7-\delta}$. *Phys. Rev. Lett.* **73**, 593 (1994).
- S12. Y. Maeno *et al.*, Two-dimensional fermi liquid behavior of the superconductor Sr_2RuO_4 . *J. Phys. Soc. Jpn.* **66**, 1405 (1997).
- S13. M. Matsumoto, M. Sigrist, Quasiparticle states near the surface and the domain wall in a $p_x \pm ip_y$ -wave superconductor. *J. Phys. Soc. Jpn.* **68**, 994 (1999).
- S14. H.-J. Kwon, V. M. Yakovenko, K. Sengupta, How to detect edge electron states in $(\text{TMTSF})_2\text{X}$ and Sr_2RuO_4 experimentally. *Synth. Met.* **133-134**, 27 (2003).
- S15. A. J. Leggett, *Quantum liquids : Bose condensation and Cooper pairing in condensed-matter systems*. (Oxford University Press, New York, 2006), pp. 281.
- S16. J. R. Kirtley *et al.*, Upper limit on spontaneous supercurrents in Sr_2RuO_4 . *Phys. Rev. B* **76**, 014526 (2007).